

Cosmological Constraints from Strong Gravitational Lensing in Clusters of Galaxies

Eric Jullo,^{1,2} Priyamvada Natarajan,^{3*,4} Jean-Paul Kneib,²
Anson D'Aloisio,⁴ Marceau Limousin,^{2,5} Johan Richard,⁶ and Carlo Schimd²

¹Jet Propulsion Laboratory, California Institute of Technology, Pasadena, CA 91109

²Laboratoire d'Astrophysique de Marseille, CNRS, Universite de Provence, 38 rue Frederic Joliot-Curie,
13388 Marseille Cedex 13, France

³Department of Astronomy, Yale University, P. O. Box 208101, New Haven, CT 06511-8101, USA

⁴Department of Physics, Yale University, P. O. Box 208120, New Haven, CT 06520-8120, USA

⁵Dark Cosmology Centre, Niels Bohr Institute, University of Copenhagen,
Juliane Maries Vej 30, 2100 Copenhagen, Denmark

⁶Institute for Computational Cosmology, Department of Physics, Durham University,
South Road, Durham, DH1 3LE, UK

*To whom correspondence should be addressed; E-mail:priyamvada.natarajan@yale.edu.

Current efforts in observational cosmology are focused on characterizing the mass-energy content of the Universe. We present results from a geometric test based on strong lensing in galaxy clusters. Based on *Hubble Space Telescope* images and extensive ground-based spectroscopic follow-up of the massive galaxy cluster Abell 1689, we used a parametric model to simultaneously constrain the cluster mass distribution and dark energy equation of state. Combining our cosmological constraints with those from X-ray clusters and the *Wilkinson Microwave Anisotropy Probe* 5-year data gives $\Omega_m = 0.25 \pm 0.05$ and $w_x = -0.97 \pm 0.07$ which are consistent with results from other methods.

Inclusion of our method with all other techniques available brings down the current 2σ contours on the dark energy equation of state parameter w_x by about 30%.

Measurements of the Hubble diagram for Type Ia supernovae (1, 2, 3, 4) combined with constraints from the Wilkinson Microwave Anisotropy Probe (WMAP5) (5, 6), cosmic shear observations (7, 8, 9, 10, 11), cluster baryon fractions (12), cluster abundances (13) and baryon acoustic oscillations (BAO) from galaxy surveys (14, 15, 16) suggests that $\sim 72\%$ of the total energy density of the Universe is in the form of an unknown constituent with negative pressure - the so-called dark energy, that powers the measured accelerating expansion. These observations probe the equation-of-state parameter w_x , defined as the ratio of pressure to energy density, through its effect on the expansion history and structure of the Universe. The current goal of cosmology is to understand the properties of dark energy by placing tighter constraints on its equation of state. In the currently favored flat Λ CDM model ¹, dark energy is attributed to a cosmological constant, for which $w_x = -1$. Type Ia supernovae, baryon acoustic oscillations, cluster abundances and cosmic shear appear to be very promising techniques to tighten constraints on the equation-of-state parameter in the near future. Because all of these techniques have biases, systematics and degeneracies, it is only in combination that robust estimates of cosmological parameters can be obtained.

The most recent census from a combination of techniques suggests that $\sim 72\%$ of the energy density in the Universe is in the form of dark energy that is powering the accelerating expansion of the Universe. In the progression towards In this work, we present results from a technique that exploits the strong gravitational lensing of distant background galaxies by massive galaxy clusters. Through their effect on the local space-time geometry, massive foreground

¹The currently favored ‘concordance’ cosmological model that best describes the Universe is the Λ CDM paradigm in which the bulk of the matter and energy density are dominated by dark matter and dark energy with baryons contributing only $\sim 5\%$.

structures cause the deflection and shearing of light rays originating from distant sources. In the case of strong lensing, the light beams are deflected so strongly that they can often result in the observation of several distorted images of a given single background galaxy. The positions of these multiple images depend strongly on the detailed properties of the lens mass distribution (17, 18, 19). Because the image positions also depend on the angular diameter distance ratios between the lens, source and observer, they encapsulate information about the underlying cosmology. We capitalize on this dependence on the geometry to derive constraints on the cosmological parameters Ω_m (the mean matter density) and w_x .

Constraining the energy content of the Universe using multiple sets of arcs in cluster lenses has been explored in the past (20, 21, 22, 23, 24, 25, 26). In particular, simultaneous inversion of the lens and derivation of cosmological constraints can be performed based on the cosmological sensitivity of the angular size-redshift relation with sources at distinct redshifts (21). In this method, the angular diameter distance ratios for 2 images from different sources defines the ‘family ratio’ Ξ , from the cosmological dependence of which constraints on Ω_m and w_x are extracted:

$$\Xi(z_l, z_{s1}, z_{s2}; \Omega_M, \Omega_X, w_X) = \frac{D(z_l, z_{s1}) D(0, z_{s2})}{D(0, z_{s1}) D(z_l, z_{s2})} \quad (1)$$

where z_l is the lens redshift, z_{s1} and z_{s2} are the two source redshifts, and $D(z_1, z_2)$ is the angular diameter distance.

Application of this method to the cluster Abell 2218 using 4 multiple image systems at distinct redshifts, resulted in $\Omega_m < 0.37$ and $w_x < -0.80$ for a flat Universe (25). A recent feasibility study demonstrates that the degeneracies of this technique are entirely distinct from those of other cluster methods and that combining the results from several simulated clusters with > 10 multiple image families in each can provide a powerful probe of dark energy (26).

We have applied this technique to the massive, lensing cluster Abell 1689 at redshift $z = 0.184$. Based on images from the Advanced Camera for Surveys (ACS) aboard the Hubble

Space Telescope (*HST*) this cluster has 114 multiple images from 34 unique background galaxies, 24 of which have secure spectroscopic redshifts (ranging from $z \sim 1$ to $z \sim 5$) obtained with the Very Large Telescope (VLT) and Keck Telescope spectrographs (27, 28). Abell 1689 is amongst the richest clusters in terms of the number density of galaxies in its core. It is also amongst the most luminous of galaxy clusters in X-ray wavelengths, with an absolute X-ray luminosity of $L_X = 20.74 \times 10^{37}$ W (29). Observationally, Abell 1689 consists of two groups of galaxies : a dominant one located at the center coincident with the peak of X-ray emission, and a secondary concentration about 1 arcminute North-East of the main one. Studies have shown that this second northern group is at a slightly higher redshift, suggesting thus that these two groups might actually be merging (30). The projected mass enhancement produced by such a merging configuration, could therefore explain the stunningly large number of multiple images identified in this cluster. Previous work shows that the mass distribution of Abell 1689 is well modeled with a set of parameterized elliptical pseudo-isothermal lensing potentials (28). We utilized the most recent parametric model of Abell 1689, which is able to reproduce the observed image configurations to within an average positional accuracy of 2.87 arcseconds, assuming a Λ CDM cosmology. We solved the lens equation in the source plane for Abell 1689 as it is computationally efficient. Inverting in the lens (image) plane provides additional information but is computationally prohibitive at present (28). Our simplified model that has a total of 21 free parameters consists of two large-scale potentials, a galaxy-scale potential for the central brightest cluster galaxy (BCG), and includes the modeling of 58 of the brightest cluster galaxies. Therefore, we explicitly include the effect of substructure in the lens plane and assigned potentials associated with bright cluster galaxies. The velocity dispersion and scale radii of all but one (the BCG) of the cluster galaxies were assumed to follow empirically motivated scaling relations, which have been previously utilized to model cluster lenses (31, 32).

Despite the large number of multiple images observed, not all of them can be utilized to

constrain cosmology. From the initial 114 images, we only used those (i) with robust, measured spectroscopic redshifts; and (ii) excluded those in the regions of the cluster with low S/N in the mass reconstruction. This selection results in the culling of multiple images that lie in the most uncertain regions of the mass distribution. Moreover, we identified several bright spots in some well resolved multiple images, which we used to increase the number of families. Applying criterion (i), resulted in a catalog of 102 images. Imposing criteria (i) and (ii), we obtained a catalog of 28 images arising from 12 families all with measured spectroscopic redshifts (Fig. 4), providing a total of 32 constraints. We assume flatness as a prior ($\Omega_{\text{tot}} = 1$) and fix the Hubble parameter at $H_0 = 74 \text{ km/s/Mpc}$ (33), as our cosmography test is not sensitive to the value of the Hubble parameter.

For each of the observed image systems with n images, we determine the goodness of fit for a particular set of model parameters using a source plane χ^2 ,

$$\chi^2 = \sum_{i=1}^n \frac{[M(\vec{\beta}_i - \langle \vec{\beta} \rangle)]^2}{\sigma_i^2}, \quad (2)$$

where $\vec{\beta}_i$ is the source plane position corresponding to image i , $\langle \vec{\beta} \rangle$ is the family barycenter, M is the magnification tensor, and σ_i is the total (observational and modeling) error. The total χ^2 was obtained by summing over families and was used in conjunction with a Markov Chain Monte Carlo (MCMC) sampler to probe the posterior probability density function (PDF) as a function of all relevant model parameters (34) (SOM). The key degeneracies with cosmological parameters for this technique arise from the velocity dispersions, ellipticity and core radii of the large scale mass clumps in the model (Fig. S4).

The angular resolution of *HST* images is on the order of 0.1 arcseconds. However, the modeling errors are generally larger due to the complexity of the cluster mass distribution, as well as the effect of intervening structures along the line of sight. We quantified the errors due to the presence of structure along the line of sight using the Millennium Simulation halo

catalogs (35). We quantified the errors on an image by image basis. By randomly slicing through snapshots of the simulation and tiling them at redshift planes between the observer and the source, we constructed 1000 line-of-sight realizations. We then ray traced through each realization with the Abell 1689 model included to estimate the effect of intervening halos on image positions. In most cases, these line-of-sight halos perturbed image positions but did not alter the multiplicity of the images. These perturbations induce positional displacements of the order of 1 arcsecond. Therefore, about 1 arcsecond of the error between observed image positions and model image predictions can be attributed to the presence of structure along the line of sight behind the cluster. The presence of projected correlated and associated large-scale structure (filaments) increases the cross-section to strong gravitational lensing making these clusters more efficient lenses, however, simulations show that this is a sub-dominant effect to that of unassociated distant large-scale structure. Therefore, the presence of aligned correlated large scale structure at the redshift of the cluster does not scupper the recovery of cosmological parameters ².

Earlier work on reconstructing the mass distribution of several massive lensing clusters, shows that the association of dark matter substructures with the locations of the brightest cluster galaxies is well matched by that derived from the Millenium Simulation (36, 32). This supports our use of luminosity-mass scaling relations to map substructure in the cluster.

The second potential source of error arises from modeling uncertainties for the substructure in the lens plane. This is likely due to scatter in the assumed scaling relations for the velocity dispersions and scale radii of cluster galaxies. Although the mean correlations between these variables may be well described by simple scaling relations, individual galaxies can deviate substantially from them, introducing errors into the parameter recovery. In order to quantify

²Filaments aligned at finite inclinations behind the cluster (thus breaking azimuthal symmetry) do yield larger deviations between the projected and multi-plane models compared to the symmetric case. For the non-symmetric case, the deviations are typically on the same level as the errors due to scatter in the cluster galaxy properties. These deviations are still subdominant to the effects of uncorrelated line-of-sight (LOS) halos.

these modeling errors, we performed Monte Carlo simulations of the lens system assuming a 20% scatter in the galaxy scaling relations. This scatter induced modeling errors on the background galaxy image positions that in some cases were as large as ~ 1 arcsecond. Therefore, the estimated errors from substructure effects in the lens plane and along the line of sight are comparable for the selected multiple image families in Abell 1689.

We use the catalog of 102 images (including images with photometric redshift estimates) and our estimates of the observational and modeling errors to obtain the marginalised PDF in the $\Omega_m - w_x$ plane. Adding in quadrature the systematic errors identified above to the positional uncertainties, results in a best model for Abell 1689 with a well defined though broad degeneracy between Ω_m and w_x . The "concordance" model of $\Omega_m \sim 0.3$ and $w_x \sim -1$ lies within the 1σ contour, but the way the degeneracy is pushed against the prior limits suggests either a bias in the mass modeling, or misidentified images (Fig. S5). Our simulations show that the errors in photometric redshift determination methods at present are too large and limit the efficiency of our technique and introduce biases (see SOM). Therefore, we excluded all images with photometric redshifts in our modeling, bringing down the number of image families used from 34 to 24. Even with this cut, some images were badly reproduced with very high RMS positional deviations, in particular, those that lie in complex crowded regions of the cluster (regions where the signal-to-noise of the mass map is low due to the presence of several bright cluster galaxies in close proximity). These outlier images from 16 families highlight complex regions in the lens mass distribution, not handled adequately by our simple parametric model. The outlier image systems also tend to have higher redshifts; thus they are likely to be more affected by uncertainties in modeling the intervening line of sight structure as well. We thus deliberately disregarded images that lie in the most complex regions in the mass distribution. While the recovery of cosmological parameters is insensitive to the choice of profile, both the PIEMD (Pseudo-Isothermal Elliptical Mass Distribution) and NFW (Navarro-Frenk-White)

provide comparable constraints on w_x and Ω_m (Fig S3), observationally some clusters are better fit to one or the other model. Abell 1689 is best fit with a PIEMD profile. The final culled image catalog thus contains 28 images, derived from 12 families at redshifts ranging from $z_S = 1.15$ to $z_S = 4.86$, all of which are spectroscopically measured (Table S1 and Fig. 4).

Optimising our model with all the spectroscopically selected images, including outlier images does not result in significant constraints on either Ω_m and w_x and yields an averaged reduced $\chi^2 = 0.08$. This indicates that the line of sight and scaling relation errors are likely overestimated. Thus, we optimized again but this time excluding the outlier images. In this iteration, we obtained an averaged reduced $\chi^2 \sim 28$, indicating that now the errors were somewhat underestimated (Fig. 8). Owing to the large estimates for the modeling errors, constraints obtained in this fashion from a single cluster lens are fairly modest. However, combining our results with those from X-ray clusters and *WMAP5* leads to $\Omega_m = 0.25 \pm 0.05$ and $w_x = -0.97 \pm 0.07$ (Fig. 8), which is consistent with the values derived from combining *WMAP5* with SN and BAO, $\Omega_m = 0.265 \pm 0.16 \pm 0.025$ and $w_x = -0.96 \pm 0.06 \pm 0.12$ (37).

Our results when combined with the results from *WMAP5* (38), the supernovae ‘‘Gold sample’’ (4), SNLS project (39) and SNEssence, and the BAO peak from *SDSS* (16), give $0.23 < \Omega_m < 0.33$ and $-1.12 < w_x < -0.82$ at the 99% confidence level (Fig. 3). This combination of all current viable probes brings down the overall error in w_x by about 30%. Therefore, the combination of cluster methods with *WMAP5* has comparable potency to the combination of other cosmological probes.

References and Notes

1. A. G. Riess, *et al.*, *AJ* **116**, 1009 (1998).
2. S. Perlmutter, *et al.*, *Nature* **391**, 51 (1998).

3. J. L. Tonry, *et al.*, *ApJ* **594**, 1 (2003).
4. A. G. Riess, *et al.*, *ApJ* **607**, 665 (2004).
5. D. N. Spergel, *et al.*, *ApJS* **170**, 377 (2007).
6. G. Hinshaw, *et al.*, *ArXiv e-prints* **803** (2008).
7. D. J. Bacon, A. R. Refregier, R. S. Ellis, *MNRAS* **318**, 625 (2000).
8. N. Kaiser, G. Wilson, G. A. Luppino, *ArXiv e-prints astro-ph/0003338* (2000).
9. L. Van Waerbeke, *et al.*, *A&A* **358**, 30 (2000).
10. D. M. Wittman, J. A. Tyson, D. Kirkman, I. Dell'Antonio, G. Bernstein, *Nature* **405**, 143 (2000).
11. E. Semboloni, *et al.*, *A&A* **452**, 51 (2006).
12. S. W. Allen, R. W. Schmidt, H. Ebeling, A. C. Fabian, L. van Speybroeck, *MNRAS* **353**, 457 (2004).
13. A. Vikhlinin, *et al.*, *ApJ* **692**, 1060 (2009).
14. G. Efstathiou, *et al.*, *MNRAS* **330**, L29 (2002).
15. U. Seljak, *et al.*, *Phys. Rev. D* **71**, 103515 (2005).
16. D. J. Eisenstein, *et al.*, *ApJ* **633**, 560 (2005).
17. J.-P. Kneib, R. S. Ellis, I. Smail, W. J. Couch, R. M. Sharples, *ApJ* **471**, 643 (1996).
18. P. Natarajan, J.-P. Kneib, I. Smail, R. S. Ellis, *ApJ* **499**, 600 (1998).
19. G. P. Smith, *et al.*, *MNRAS* **359**, 417 (2005).

20. B. Paczynski, K. Gorski, *ApJ* **248**, L101 (1981).
21. R. Link, M. J. Pierce, *ApJ* **502**, 63 (1998).
22. A. R. Cooray, J. M. Quashnock, M. C. Miller, *ApJ* **511**, 562 (1999).
23. G. Golse, J.-P. Kneib, G. Soucail, *A&A* **387**, 788 (2002).
24. M. Sereno, *A&A* **393**, 757 (2002).
25. G. Soucail, J.-P. Kneib, G. Golse, *A&A* **417**, L33 (2004).
26. J. Gilmore, P. Natarajan, *MNRAS* **396**, 354 (2009).
27. T. Broadhurst, N. Benítez, D. Coe, et al, *ApJ* **621**, 53 (2005).
28. M. Limousin, *et al.*, *ApJ* **668**, 643 (2007).
29. H. Ebeling, *et al.*, *MNRAS* **281**, 799 (1996).
30. O. Czoske, *IAU Colloq. 195: Outskirts of Galaxy Clusters: Intense Life in the Suburbs*, A. Diaferio, ed. (2004), pp. 183–187.
31. P. Natarajan, J.-P. Kneib, *MNRAS* **287**, 833 (1997).
32. P. Natarajan, *et al.*, *ApJ* **693**, 970 (2009).
33. S. H. Suyu, *et al.*, *ArXiv e-prints 0910.2773* (2009).
34. E. Jullo, *et al.*, *New Journal of Physics* **9**, 447 (2007).
35. V. Springel, C. S. Frenk, S. D. M. White, *Nature* **440**, 1137 (2006).
36. P. Natarajan, G. De Lucia, V. Springel, *MNRAS* **376**, 180 (2007).

37. R. Kessler, *et al.*, *ApJS* **185**, 32 (2009).
38. E. Komatsu, *et al.*, *ApJS* **180**, 330 (2009).
39. P. Astier, *et al.*, *A&A* **447**, 31 (2006).
40. A. Kassiola, I. Kovner, *ApJ* **417**, 450 (1993).
41. S. M. Faber, R. E. Jackson, *ApJ* **204**, 668 (1976).
42. S. Wuyts, P. G. van Dokkum, D. D. Kelson, M. Franx, G. D. Illingworth, *ApJ* **605**, 677 (2004).
43. A. Fritz, B. L. Ziegler, R. G. Bower, I. Smail, R. L. Davies, *MNRAS* **358**, 233 (2005).
44. L. V. E. Koopmans, T. Treu, A. S. Bolton, S. Burles, L. A. Moustakas, *ApJ* **649**, 599 (2006).
45. M. S. Turner, M. White, *Phys. Rev. D* **56**, 4439 (1997).
46. T. Broadhurst, *et al.*, *ApJ* **619**, L143 (2005).
47. M. Oguri, M. Takada, K. Umetsu, T. Broadhurst, *ApJ* **632**, 841 (2005).

40. EJ and JPK acknowledge fruitful discussions with D. Coe, L. Koopmans, L. Moustakas and M. Auger. The authors are thankful for computational resources from IDRIS/CNRS, JPL and J.-C Bourret. EJ acknowledges a NASA post-doctoral fellowship; and PN acknowledges a Radcliffe Fellowship at Harvard. JPK, ML and CS acknowledge support from CNRS; and ML thanks CNES & Ville de Marseille. The authors thank Alexey Vikhlinin for providing data on cosmological constraints from X-ray clusters to combine with our strong lensing results.

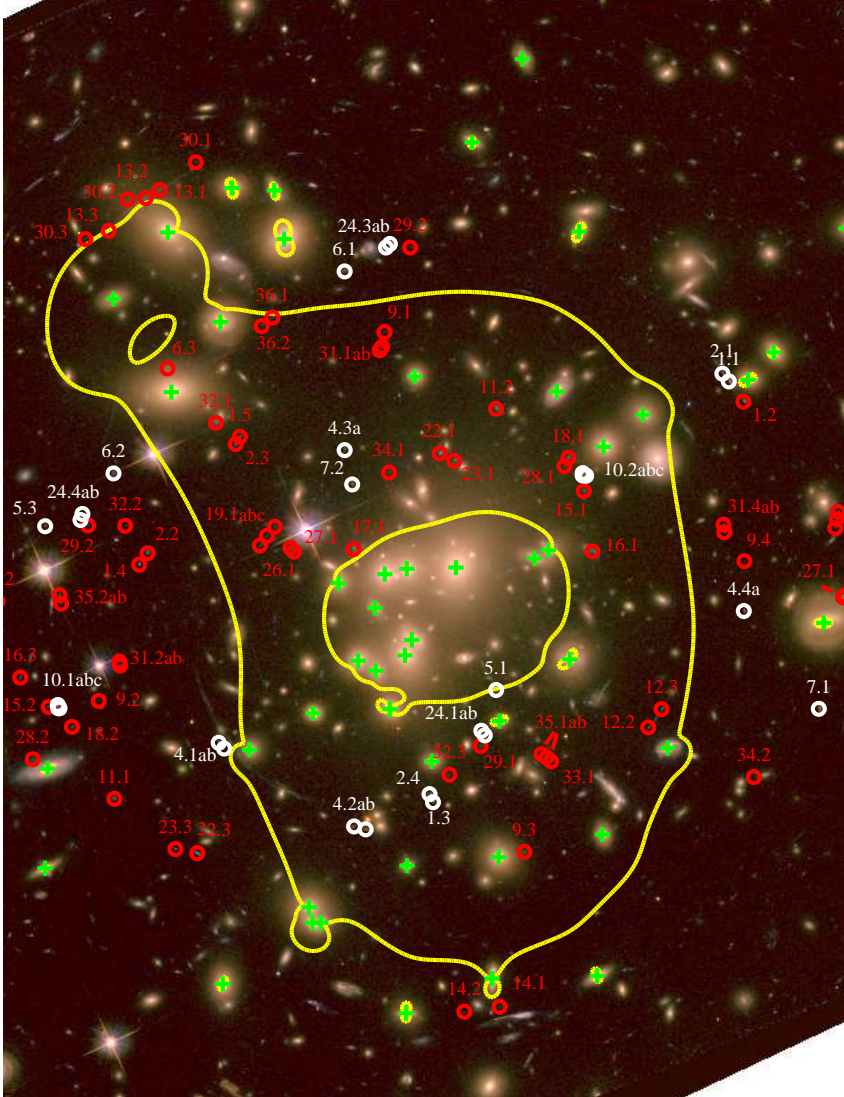


Figure 1: The critical lines for a source at $z = 3$ are overplotted in yellow on the *HST ACS* image of Abell 1689. The lensing mass model used is the one from which we derived cosmological constraints. In addition to 2 large scale clumps and the BCG, this model includes the contribution of 58 cluster galaxies. The positions of cluster galaxies are marked with green crosses. Overplotted in white are the 28 multiple images arising from 12 families that we used in this work; the red circles mark the positions of the rejected images.

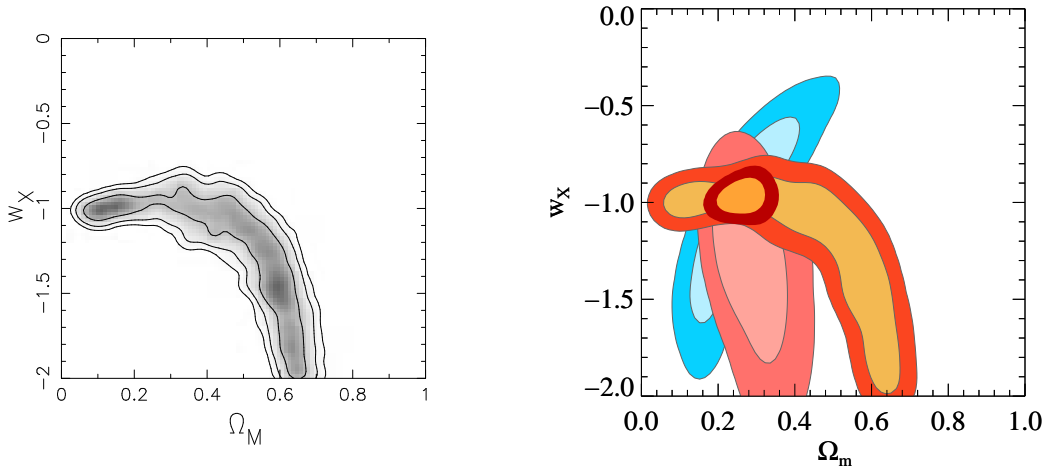


Figure 2: Left) The results from the simultaneous Bayesian optimization of the detailed mass distribution and cosmological parameters in the $\Omega_m - w_x$ plane for Abell 1689 using the 28 multiple images belonging to 12 families at distinct redshifts as constraints from strong lensing including only observational errors. The plotted contours are the 1, 2 and 3- σ confidence levels. (Right) The results from combining cosmological constraints from *WMAP5*+ evolution of X-ray clusters +cluster strong lensing (cluster only methods); the 1 and 2 σ contours are plotted, blue contours - constraints from *WMAP5*, pink contours - X-ray clusters, orange contours - cluster strong lensing. We multiplied the likelihoods for the various techniques to obtain this plot. The degeneracy directions for X-ray clusters and cluster strong lensing are orthogonal.

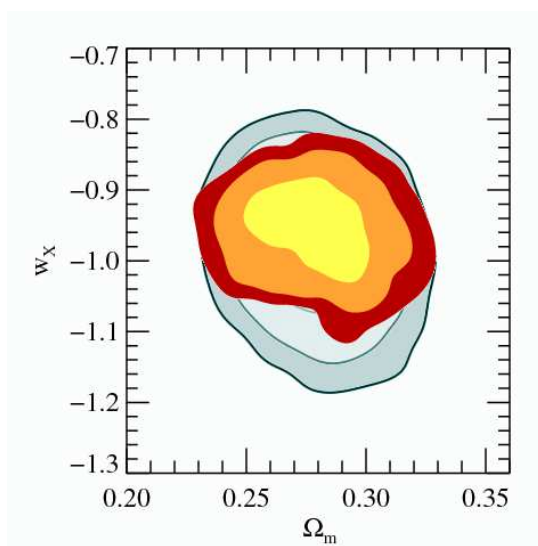


Figure 3: Combination of constraints from strong lensing, the *WMAP5* data (38), the supernovae “Gold sample” (4), SNLS project (39) and SNEssence, and the BAO peak from *SDSS* (16). Contours for non-SL cosmological probes come from the *WMAP* plotter. The overplotted contours are all 1, 2 and 3- σ confidence levels.

Supporting Online Materials

Mass reconstruction of Abell 1689

As a starting point for the cosmography work, we use the strong lensing based mass model presented in Limousin et al. 2007. We summarize this model briefly below. The mass distribution in Abell 1689 was reconstructed in a parametric fashion using detected strong lensing features from deep *HST* ACS observations and extensive ground based spectroscopy. We find 36 multiply imaged systems yielding 102 images, of which 24 systems have reliably determined spectroscopic redshifts. These systems span a redshift range between $z = 1.1$ and $z = 4.9$ and provide a total of 136 constraints for the analysis. The multiple images used and their relevant properties, including location and redshift are shown in Table 1. The resulting mass distribution in this cluster is found to be bimodal: the dominant component is a central large scale mass clump/halo coincident with the location of the brightest cluster galaxy (BCG) and the center of the X-ray emission. The second mass component is a another large scale mass clump/halo in the north-east part of the ACS field, it also contributes substantially to the overall mass distribution and is required by the data to reproduce several of the multiple image geometries. In addition, this model includes the galaxy scale dark matter haloes associated with the all the identified cluster members (totalling 267) detected within the ACS field providing the smaller scale structure in the dark matter distribution. The critical lines for this mass model are shown in Figure 4. To keep the mass model simple and yet include the contribution of small scale structure, standard scaling laws with luminosity are assumed for the cluster galaxies. Thus the final mass model has 33 free parameters. The large number of observational constraints used (136 constraints) makes Abell 1689 the most reliably reconstructed cluster to date, with a mass distribution constrained at the per cent level, a level required in order to exploit Abell 1689 efficiently as a cosmological probe. **Note that this is the baseline input mass model that we**

started with, eventually, to extract cosmological parameters we pared down the model to include only 58 of the cluster galaxies and only 28 images all with measured spectroscopic redshifts. Details of the selection are presented in the paper.

Strong lensing modeling

Although numerical simulations suggest that dark matter halos are well described by the spherically averaged universal Navarro-Frenk-White (NFW) density profile, in lensing studies we routinely prefer the truncated Pseudo Isothermal Elliptical Mass Distribution (PIEMD) potentials (40) for the extra degree of freedom in allowing ellipticity and due to fact that these models have finite mass. The 3-dimensional PIEMD density distribution is given by:

$$\rho(r) = \frac{\rho_0}{(1 + r^2/r_{core}^2)(1 + r^2/r_{cut}^2)}. \quad (3)$$

The PIEMD potential is parameterised by a central density, ρ_0 , related to the central velocity dispersion of the potential, σ_0 , and two characteristic radii that define the scales on which the slope of the density profile changes. The profile is flat in the inner region, then isothermal ($\rho \simeq r^{-2}$) between r_{core} and r_{cut} , and steeply decreases ($\rho \simeq r^{-4}$) beyond r_{cut} . In addition, the ellipticity ϵ and the position angle θ further characterise the shape of the potential. The PIEMD potential has been extensively and successfully used to model galaxy clusters (17, 19, 28).

In the inner regions of clusters that are pertinent to the calculation of strong lensing effects, cluster galaxies are mostly early-type galaxies, and have been found to follow the scaling relations like the Faber-Jackson relation (41, 42, 43). Utilizing these observed empirical scalings in our models, we assume that the masses of cluster galaxies scale with their luminosity L , via the following scaling relations:

$$r_{core} = r_{core}^* (L/L^*)^{1/2}, \quad r_{cut} = r_{cut}^* (L/L^*)^{1/2}, \quad \sigma_0 = \sigma_0^* (L/L^*)^{1/4} \quad (4)$$

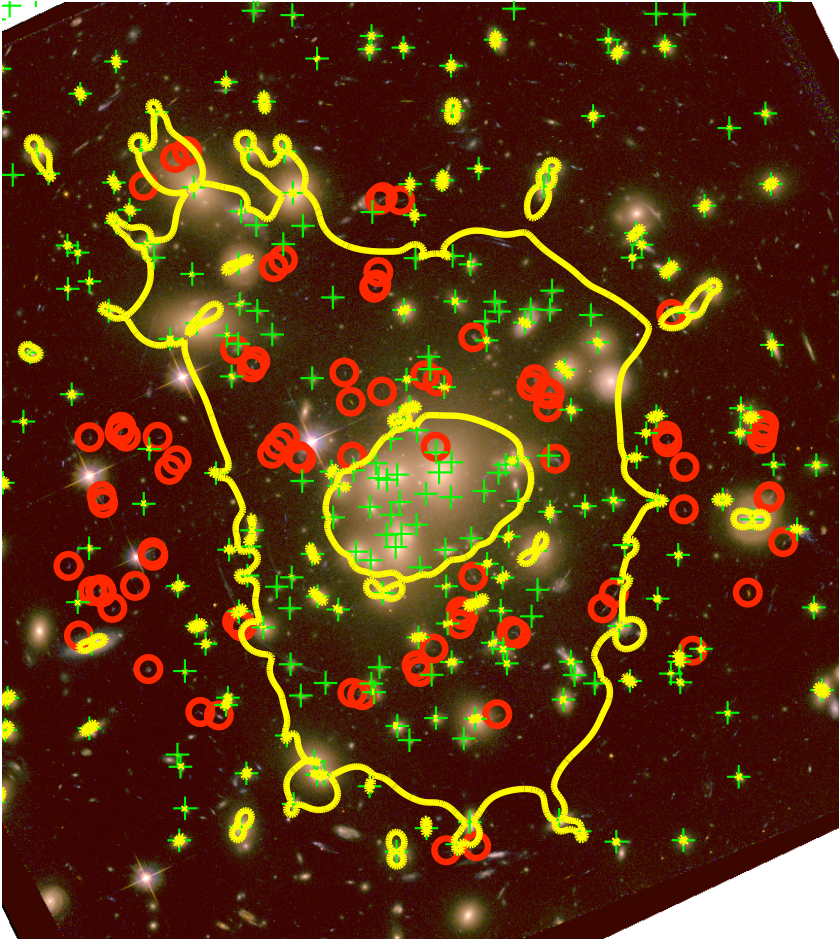


Figure 4: Mass model for Abell 1689 published in Limousin et al. (2007): the critical lines for a source at $z = 3$ are overplotted in yellow on the *HST* ACS image of Abell 1689. This is done for the best-fit lensing mass model that includes 267 cluster galaxies. Overplotted in red are all the multiple images including those with photo-metric redshifts. Cluster members selected in Abell 1689 using the color-magnitude relation are marked with green crosses.

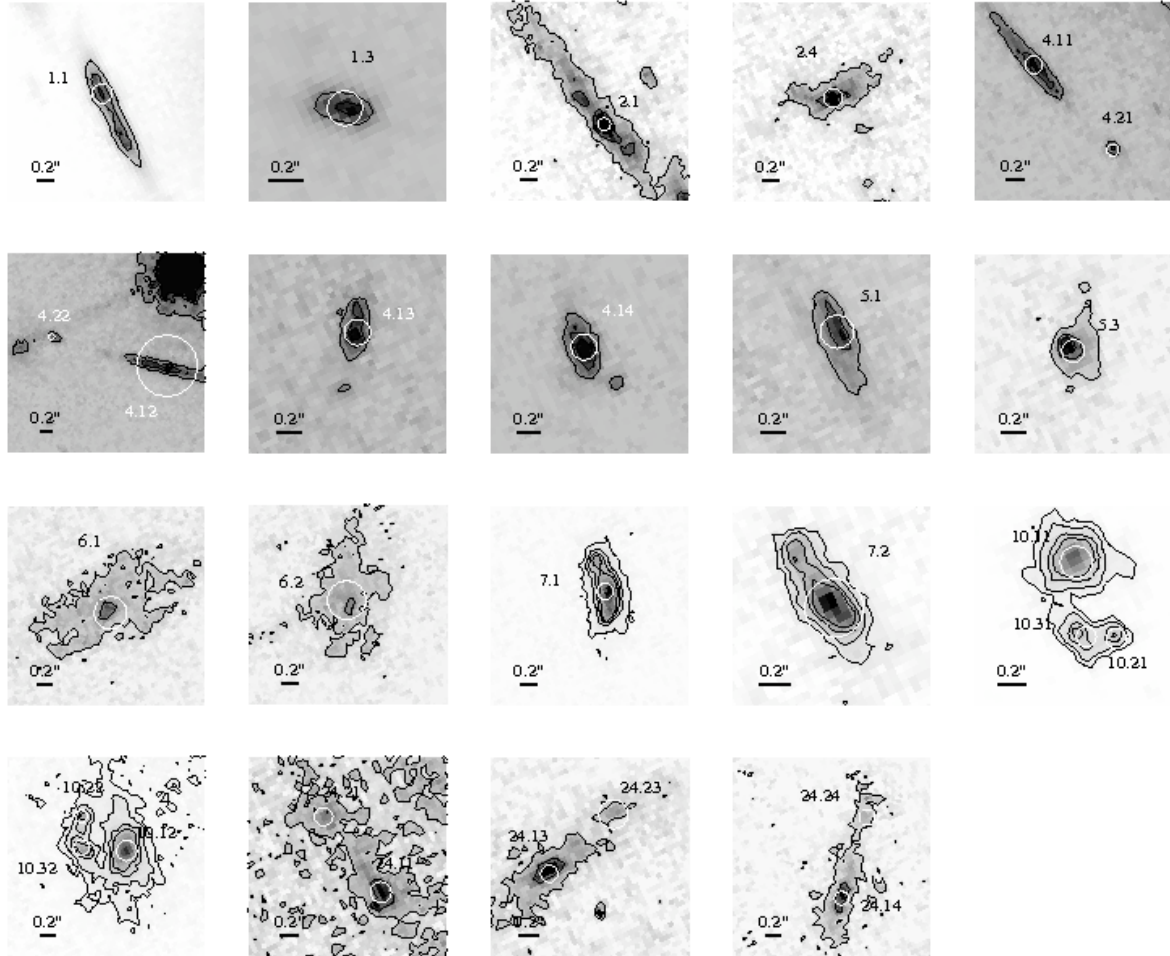


Figure 5: The identification of multiple images in Abell 1689 from the high resolution *HST* ACS data: shown are a few examples wherein the white circle plotted is the positional accuracy of each image. The images are labeled as A.B where A denotes the family number and B the image number within family A. Note that even within a given family of images of the same source, the error varies due to the variation in S/N of the images determined by the background that in turn depends on the location of the images.

ID	R.A.	Decl.	z	σ_x	σ_y	RMS
1.1	13:11:26.45	-1:19:56.38	3.050	0.11	0.11	0.57
1.3	13:11:29.77	-1:21:07.32	3.050	0.10	0.10	0.17
2.1	13:11:26.52	-1:19:55.08	2.533	0.07	0.07	0.30
2.4	13:11:29.81	-1:21:05.96	2.533	0.11	0.11	0.34
4.1a	13:11:32.17	-1:20:57.34	1.1648	0.10	0.10	0.47
4.1b	13:11:32.11	-1:20:58.31	1.1648	0.07	0.07	0.44
4.2a	13:11:30.52	-1:21:11.90	1.1648	0.52	0.52	1.27
4.2b	13:11:30.65	-1:21:11.41	1.1648	0.05	0.05	0.48
4.3a	13:11:30.76	-1:20:08.01	1.1648	0.11	0.11	0.41
4.4a	13:11:26.28	-1:20:35.06	1.1648	0.11	0.11	0.27
5.1	13:11:29.06	-1:20:48.41	2.636	0.14	0.14	1.59
5.3	13:11:34.11	-1:20:20.88	2.636	0.10	0.10	0.27
6.1	13:11:30.76	-1:19:37.90	1.15	0.21	0.21	3.28
6.2	13:11:33.35	-1:20:11.97	1.15	0.24	0.24	1.23
7.1	13:11:25.44	-1:20:51.53	4.86	0.10	0.10	0.56
7.2	13:11:30.67	-1:20:13.80	4.86	0.19	0.19	0.46
10.1a	13:11:33.97	-1:20:51.00	1.830	0.12	0.12	0.13
10.1b	13:11:33.95	-1:20:51.55	1.830	0.07	0.07	0.21
10.1c	13:11:33.96	-1:20:51.54	1.830	0.07	0.07	0.18
10.2a	13:11:28.05	-1:20:12.29	1.830	0.13	0.13	0.22
10.2b	13:11:28.09	-1:20:11.85	1.830	0.08	0.08	0.32
10.2c	13:11:28.09	-1:20:12.24	1.830	0.10	0.10	0.27
24.1a	13:11:29.19	-1:20:56.05	2.63	0.10	0.10	0.42
24.1b	13:11:29.22	-1:20:55.28	2.63	0.09	0.09	0.31
24.3a	13:11:30.29	-1:19:33.87	2.63	0.09	0.09	0.85
24.3b	13:11:30.25	-1:19:33.27	2.63	0.15	0.15	1.31
24.4a	13:11:33.72	-1:20:19.82	2.63	0.09	0.09	0.17
24.4b	13:11:33.69	-1:20:18.80	2.63	0.10	0.10	0.11

Table 1: Catalog of 28 images used in this work to constrain cosmology. The columns are ID, R.A., Decl., z, x (positional uncertainty in CCD row), y (positional uncertainty in CCD column), RMS (error between predicted and observed image positions). All images have secure spectroscopic redshifts.

where L^* is the luminosity of a typical galaxy in the cluster; r_{core} is fixed to an arbitrary small value of 0.15 kpc; r_{cut}^* and σ_0^* depend on the properties of the cluster and are left as free parameters. The small value of r_{core} is in agreement with the results of (44), from the modeling of individual lensing galaxies wherein it appears that early-type galaxies are isothermal in their inner regions. According to these definitions, the halo mass is proportional to $\sigma_0^2 r_{cut}$ and the mass-to-light ratio is constant (31).

Cosmological angular diameter distances are modeled according to the definition from (45) as,

$$D_A = \frac{cH_0^{-1}}{1+z} \int_{z_1}^{z_2} dz \left(\Omega_m(1+z)^3 + (1+z)^{3(w_x+1)}\Omega_x \right)^{-1/2}. \quad (5)$$

In this equation, we assume a flat Universe (choice of prior). In addition, since we assume matter and dark energy to be the only significant components in the Universe, the sum of their respective parameters $\Omega_m + \Omega_x = 1$. Finally, we assume the Hubble constant to be $H_0 = 74 \text{ km/s/Mpc}$ (33). As for the two cosmological parameters (Ω_m, w_x) , we assign the following uniform priors $\Omega_m \in [0, 1]$ and $w_x \in [-2, 0]$.

In optical images, galaxies in Abell 1689 form 2 groups : one predominantly in the centre, and the second located about one arcminute to the North-East. As in (28), our final model for Abell 1689 consists of 2 cluster-scale halos, one galaxy-scale halo to model the BCG at the center of the dominant group. On top of that, we add the color-magnitude selected catalog of cluster member galaxies from (28), but with an additional cut in deflection angle. Only halos that produce a deflection larger than 0.07 arcsecond (i.e. about half the observational uncertainty on the image positions) are selected. Thus, we obtain a catalog of 58 cluster member galaxies brighter than $m_K < 18.11$. Each galaxy is assigned a PIEMD potential and the scaling relations outlined above are adopted. In total, our final mass model has a total of 21 free parameters, with 124 image constraints. The adopted best estimate values for the mass model parameters are reported in Table 2.

Cluster Mass component	Δ R.A. ^a (arcsec)	Δ Decl. ^a (arcsec)	ϵ^b	θ^c (deg)	r_{core} (arcsec)	r_{cut} (arcsec)	σ_0 (km s ⁻¹)	RMS (arcsec)
Abell 1689 :								
Cluster #1	$0.5^{+0.6}_{-0.5}$	$-4.2^{+0.5}_{-0.6}$	$0.32^{+0.03}_{-0.02}$	$88.5^{+1.6}_{-1.9}$	14^{+2}_{-1}	1.5 Mpc	1249^{+29}_{-30}	2.54
Cluster #2	$-58.7^{+1.5}_{-0.5}$	$43.2^{+1.0}_{-3.5}$	$0.84^{+0.00}_{-0.01}$	125^{+2}_{-3}	$0.6^{+0.0}_{-0.3}$	1.5 Mpc	555^{+26}_{-28}	
BCG	$-6.1^{+0.9}_{-0.0}$	$-4.5^{+1.8}_{-0.0}$	0.13	85	$0.5^{+0.0}_{-0.5}$	14^{+41}_{-0}	387^{+71}_{-112}	
L* ral. → $m_K^* =$ 16	0.03	26^{+52}_{-15}	30^{+188}_{-13}	

Table 2: Estimated values and errors at 1σ confidence for the parameters of the mass model of Abell 1689; ^a the position of each mass component is given relative to the cluster centre; ^b the ellipticity corresponds to the *lenstool* input ellipticity for a PIEMD potential $\epsilon = (a^2 - b^2)/(a^2 + b^2)$, where a and b are major and minor axis of the PIEMD mass distribution; the orientation θ increases from West to North.

Before launching any computationally intensive runs with the full set of images, we perform a quick check with a scaled down version of our mass model excluding cluster member galaxies. For the two smooth cluster-scale potentials and the BCG potential, we optimise the positions, ellipticities, orientations, core radii, cut radii, and velocity dispersions. We also let Ω_m and w_x free to vary between the limits stated above. As constraints, we use two systems at redshifts 3.050 and 2.533. These are both 5-fold multiply imaged systems with most of their images located far from any bright cluster galaxy. In addition, these 2 systems form two Einstein crosses, with most of their images appearing at the same distance from the cluster center. Using these two systems, the estimated cluster mass obtained is rather insensitive to our choice of the form of the density profile. Consequently, our estimated values for Ω_m and w_x from these systems will be independent of our detailed modeling of the lens potential. We obtain a degeneracy between Ω_m and w_x in agreement with our theoretical expectations (26). Although we obtain large error bars on both Ω_m and w_x , the favored cosmological parameter values ($\Omega_m = 0.3$ and $w_x = -1$) are well centred in the 1σ contour. For all subsequent runs, we use the 3σ confidence intervals of each mass model parameter derived from this run as priors.

Note that the choice of parameterization of the mass model (NFW profile versus PIEMD) does not impact recovery of cosmological parameters. While NFW profiles are found to be a good fit to simulated massive galaxy clusters, in reality the NFW is not always the best fit to lensing data of observed galaxy clusters. From our extensive experience in modeling the mass distributions of lensing clusters combining constraints from both the strong and weak lensing regime, we find that for a majority of clusters the PIEMD (Pseudo-Isothermal elliptical mass distribution) is a significantly better fit than the NFW. This is most definitely the case for Abell 1689. In our earlier work on modeling the mass distribution of this cluster presented in Limousin et al. (2008), we investigated a range of models NFW, generalized elliptical NFW, PIEMD and power law models. Ranking model fits using Bayesian evidence derived by using the MCMC sampler we found that the PIEMD model offered the best fit to the current data. Therefore, as a starting point for the cosmography work we started with the best-fit mass model parameters which are of course then simultaneously optimised within reasonable ranges (the model is not fixed).

In order to test the role of this choice of parametric model on the recovery of cosmological parameters, we have performed detailed simulations with many realizations of both the NFW and PIEMD modeled clusters. As we show in Figure 3 the choice of mass model does not bias recovery of input parameters. In the simulations, for both mass distributions, it was assumed that we have constraints from 20 image families all with measured spectroscopic redshifts. The simulated clusters are taken to be at the same redshift $z = 0.2$, each with 20 families created from the same background source catalog: one is PIEMD and one is NFW. There are no subclumps included as the issue to settle here is the dependence of the choice of the smooth model. Typical observational errors were assumed for both cases. It turns out that the PIEMD contours are slightly wider, probably due to the additional parameter needed.

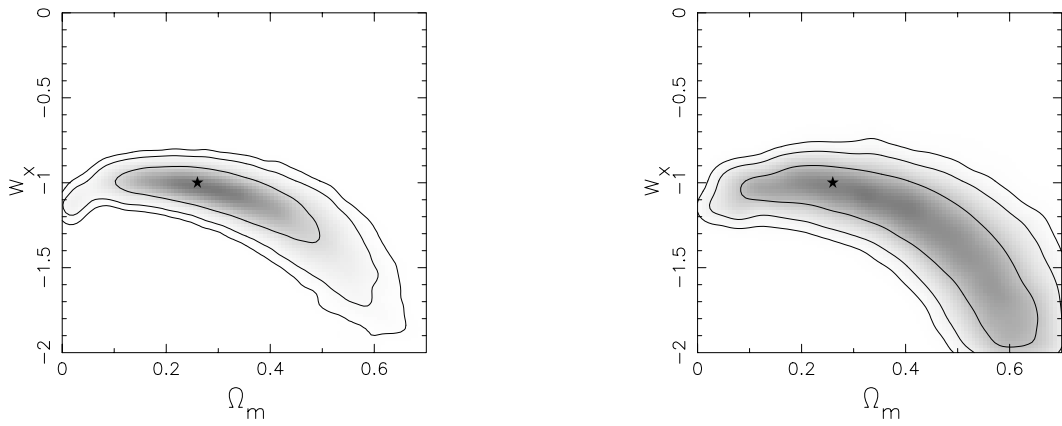


Figure 6: Left Panel: The recovery of input cosmological parameters with a simulated cluster modeled with an NFW profile utilizing 20 image families. Right Panel: The recovery with the same cluster and background image catalog as above but with a cluster modeled with a PIEMD profile.

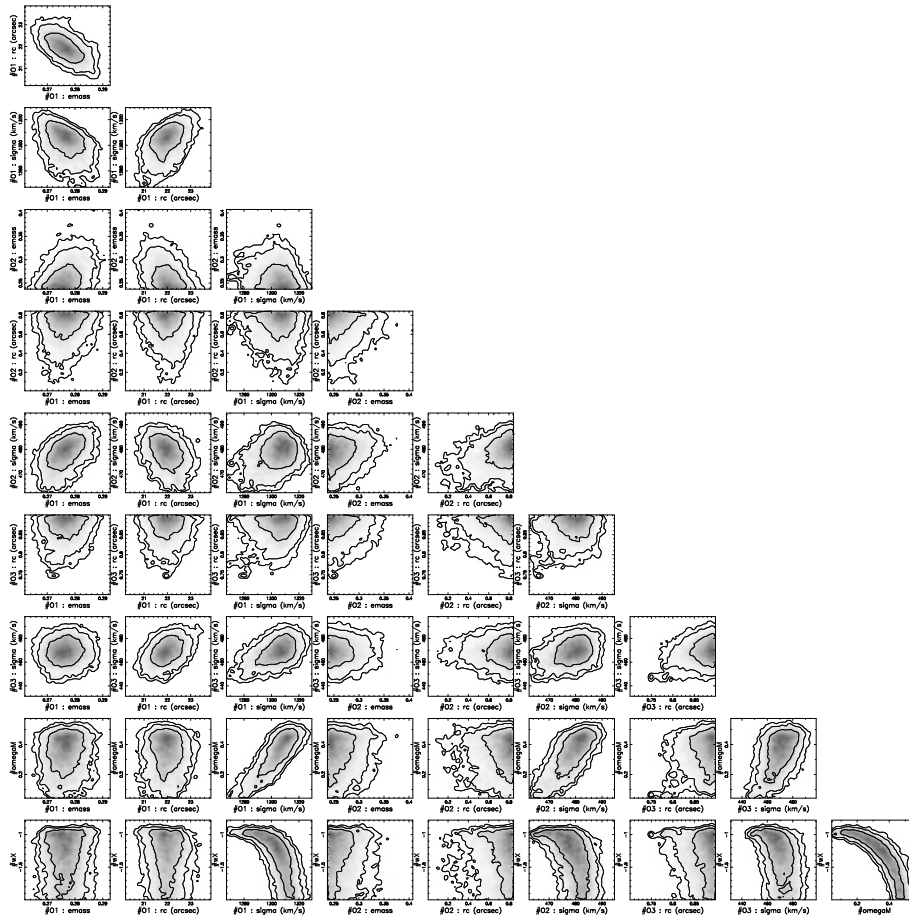


Figure 7: Tabulation of the key parameter degeneracies: cosmological parameters are degenerate with the following lens model parameters σ velocity dispersion, ellipticity and core radius. This is shown in the results from the combined Bayesian optimization of the mass distribution and cosmology in Abell 1689. In this plot, e_{mass} is the ellipticity of the mass; $r_{\text{core}} = r_c$ the core radius and σ the velocity dispersion. The 2 large-scale clumps and the BCG are denoted by 1, 2 and 3 respectively.

Inventory of systematic errors in the modeling of Abell 1689

Due to the large number of images found in Abell 1689, we can expect the constraints on cosmology to be very tight. However, it is known that parametric models are not flexible enough to reproduce all the images at the observational level of accuracy (46, 47). Moreover, an initial analysis with the 0.13 arcsecond positional uncertainty found above, yielded different modes in our parameter space with similar likelihoods that provided very different estimates for Ω_m and w_x . This often happens when systematic errors are not adequately taken into account. Therefore, we present a preliminary analysis of the systematic errors for Abell 1689 in this work. We treat two sources in this work: systematic errors arising from cluster galaxies in the lens plane and halos along the line of sight.

Substructure in the lens plane: The velocity dispersions and scale radii of cluster member galaxies are likely to display significant scatter about the scaling relations we assumed to model them. If not properly accounted for, this scatter can introduce biases into the parameter recovery. In order to quantify this effect on an individual image basis, we perform Monte Carlo simulations of the lens system. We first obtain a set of source locations by mapping each observed image back to the source plane using the initial cluster model. We randomly draw σ_0 and r_{cut} parameters for the cluster galaxies from Gaussian distributions with mean values obtained from the above scaling relations and standard deviations equal to 20 per cent of the mean. We then lens the source locations to the image plane using the cluster model with each realization of the galaxy population. We find that a 20 per cent scatter in the velocity dispersions and scale radii can induce modeling errors on the image positions that can be as large as ~ 1 arcsecond. Put in another way, in trying to avoid potential biases in the cosmological parameters, we should not expect our simplified models to reproduce image positions to within ~ 1 arcsecond given the limitations on modeling the galaxy population.

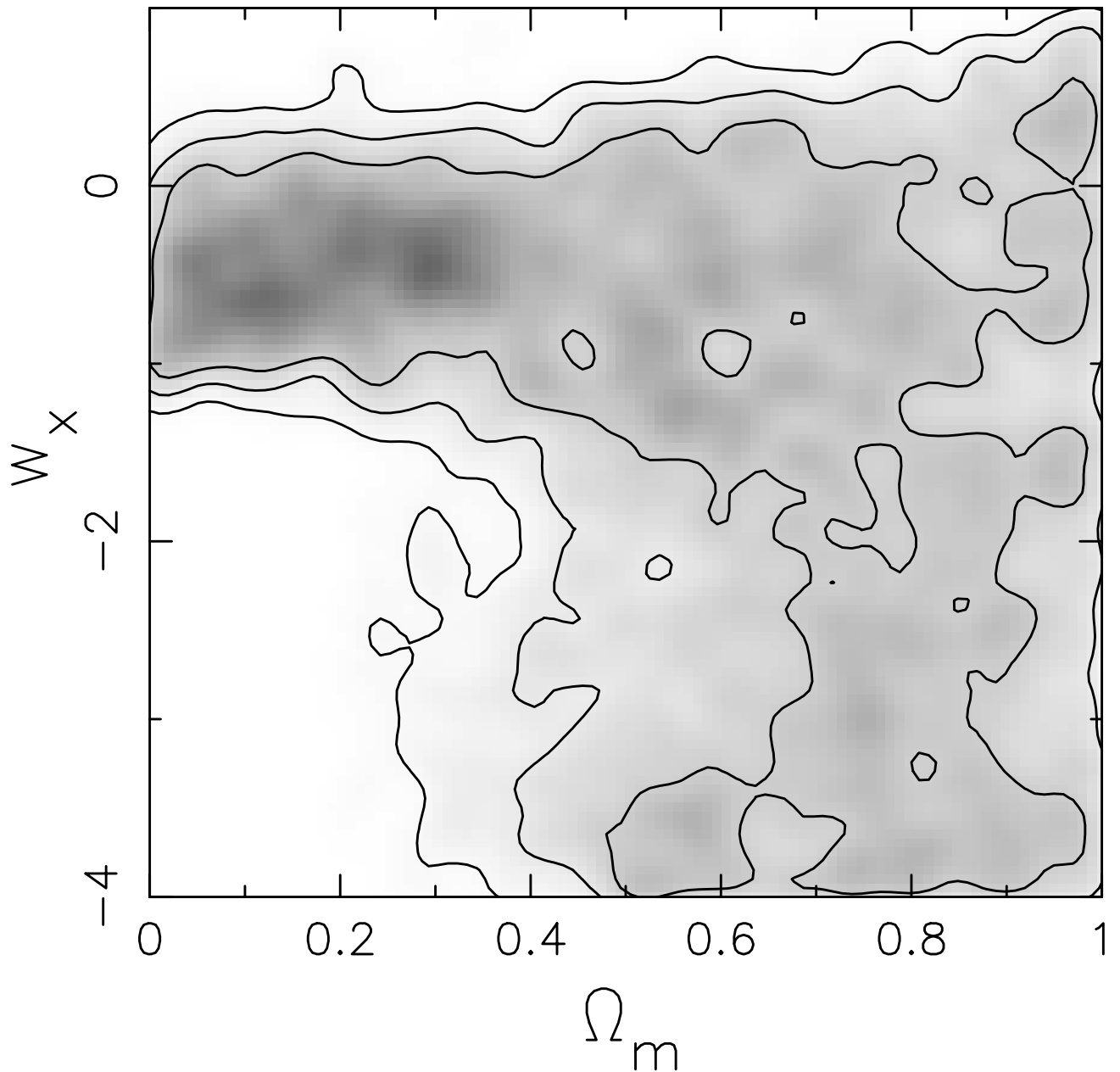


Figure 8: The results from the simultaneous Bayesian optimization of the detailed mass distribution and cosmological parameters in the $\Omega_m - w_x$ plane for Abell 1689 including all available families of multiple images as constraints including all sources of error from observations, the line of sight structure as well as errors in scaling relations employed to model cluster galaxies. For this iteration all the 102 images were used including 58 cluster galaxies, error from all systematics were added to each image. The RMS error in reconstructing image positions was large signaling that the mass model was not accurate enough.

Substructure along the line of sight: We also quantify the errors due to halos along the line of sight using the Millennium Simulation (MS) halo catalogs (35), which are freely available for download. We construct lens planes by selecting randomly oriented slices from each MS snapshot. We obtain a catalog of halo positions and masses (down to $10^{11} M_{\odot}$) in each slice and project their positions along one direction. We then place analytic NFW potentials at each halo location, using the mass and redshift to assign a concentration parameter through scaling relations obtained from N-body simulations in the literature. The lens planes are tiled along the line of sight and the cluster model is inserted at the appropriate redshift. We ray trace the sources through many line-of-sight realizations. We find that, although the line-of-sight structure only occasionally changes the multiplicity of a family, the more common effect is to simply perturb the image positions. We find that these perturbations are also typically on the order of 1 arcsecond.

We also study the effect of line of sight structure correlated with the cluster on the recovery of cosmological parameters using simulations. In our analysis, we utilize the multiple lensplane approximation. The total deflection is approximated as a series of point deflections occurring at discrete redshifts. The separation between lensplanes is typically ~ 100 Mpc. In other words, all matter within a rectangle of length ~ 100 Mpc is projected onto a plane. This is generally known to be a satisfactory approximation to treating the matter distribution as continuous. Regarding the effect of correlated large-scale structure, we note it can be reasonably modeled as sitting at the redshift of the cluster. Hence, it is reasonable to treat any correlated structure within ~ 50 Mpc as part of the projected mass of the lens itself. As an important example, we explored the effect of a long filament aligned along the line-of-sight behind the cluster. At the present, we are not able to utilize N-body simulations for this exploration. Instead, we use a simple parametric approach. We place a primary lens, representing a massive cluster (with mass $M = 1.7 \cdot 10^{15} M_{\odot}$), at $z = 0.184$. We then place 5

equivalent circular potentials, with centers at the origin, spaced 10 Mpc apart behind the cluster to represent a filament (this is equivalent to breaking up the filament into 5 lensplanes). We use PIEMD profiles for these potentials with core radii of 0.5 Mpc and cut radii of 1.5 Mpc. With these parameters, each contributing potential has a constant density inside 0.5 Mpc and drops off as r^{-2} for $r < 1.5$ Mpc. Outside of 1.5 Mpc, the density goes as r^{-4} . The total mass within the simulated filament is $10^{15} M_{\odot}$. We also create a "projected" model in which all potentials are placed on the same lensplane at $z = 0.184$.

We lensed 10 simulated source catalogs with both the projected and full models and compared the resulting images. On average, deviations between the full and projected models are around 0.6 arcsecond; less than half of the typical combined error from cluster galaxy scatter and uncorrelated LOS halos. So even in the worst-case scenario of a long filament with mass roughly equal to the cluster, with its axis aligned exactly along the line-of-sight, the error due to modeling it in the same lensplane as the cluster is subdominant to the effects we have considered in our analysis.

Bayesian MCMC approach to exploiting strong lensing observations

We start with a parametrization describing the lens, the starting point as described earlier is the best-fit model for Abell 1689 published by Limousin et al. (2008). Using LENSTOOL software we explore the parameter space around the best-fit model while simultaneously solving for the family ratio for pairs of images. This is done while reproducing the location of the observed multiple images within the supplied uncertainties. Earlier versions of the software (Kneib et al. 1993) were based on a downhill minimization. However, that technique was very sensitive to local minima in the likelihood distribution; as a result, the modeling of complex systems as seen in Abell 1689 became rapidly too inefficient. In order to tackle the

current observational data for Abell 1689, we implemented a new optimization method based on a Bayesian Markov Chain Monte Carlo (MCMC) approach. The initial assumed model defines the prior PDF from which after sampling the posterior PDF is constructed for a range of acceptable model parameters. We use the Bayesian evidence to rank the models that best reproduce systems of multiple images. The Bayesian evidence is used to rank and characterize models when scanning parameter space. More details on this procedure can be found in Jullo et al. (2008).

In terms of the actual chains used, we run 10 interlinked Markov chains at the same time to prevent any Markov chain from falling into a local minimum. The MCMC convergence to the posterior PDF is performed with a variant of the "thermodynamic integration" technique (Ruanaidh and Fitzgerald 1996) called selective annealing. Here "selective" stands for the following process. At each step, 10 new samples (one per Markov chain) are drawn randomly from the current posterior PDF (which corresponds to the prior PDF at the beginning). These samples are then weighted according to their likelihood and selected with a variant of the Metropolis-Hasting algorithm (Metropolis et al. 1953; Hastings 1970). Roughly, the samples with the worst likelihood are deleted and the ones with the best likelihood are duplicated so that we always have 10 Markov chains running at the same time. These chains are run in parallel for efficiency. This ensures that the choice of initial seed does not impact the calculation, it generates more samples yielding smoother contour plots for the cosmological parameters Ω_m and w_x .

References and Notes

1. A. G. Riess, *et al.*, *AJ* **116**, 1009 (1998).
2. S. Perlmutter, *et al.*, *Nature* **391**, 51 (1998).

3. J. L. Tonry, *et al.*, *ApJ* **594**, 1 (2003).
4. A. G. Riess, *et al.*, *ApJ* **607**, 665 (2004).
5. D. N. Spergel, *et al.*, *ApJS* **170**, 377 (2007).
6. G. Hinshaw, *et al.*, *ArXiv e-prints* **803** (2008).
7. D. J. Bacon, A. R. Refregier, R. S. Ellis, *MNRAS* **318**, 625 (2000).
8. N. Kaiser, G. Wilson, G. A. Luppino, *ArXiv e-prints astro-ph/0003338* (2000).
9. L. Van Waerbeke, *et al.*, *A&A* **358**, 30 (2000).
10. D. M. Wittman, J. A. Tyson, D. Kirkman, I. Dell'Antonio, G. Bernstein, *Nature* **405**, 143 (2000).
11. E. Semboloni, *et al.*, *A&A* **452**, 51 (2006).
12. S. W. Allen, R. W. Schmidt, H. Ebeling, A. C. Fabian, L. van Speybroeck, *MNRAS* **353**, 457 (2004).
13. A. Vikhlinin, *et al.*, *ApJ* **692**, 1060 (2009).
14. G. Efstathiou, *et al.*, *MNRAS* **330**, L29 (2002).
15. U. Seljak, *et al.*, *Phys. Rev. D* **71**, 103515 (2005).
16. D. J. Eisenstein, *et al.*, *ApJ* **633**, 560 (2005).
17. J.-P. Kneib, R. S. Ellis, I. Smail, W. J. Couch, R. M. Sharples, *ApJ* **471**, 643 (1996).
18. P. Natarajan, J.-P. Kneib, I. Smail, R. S. Ellis, *ApJ* **499**, 600 (1998).
19. G. P. Smith, *et al.*, *MNRAS* **359**, 417 (2005).

20. B. Paczynski, K. Gorski, *ApJ* **248**, L101 (1981).
21. R. Link, M. J. Pierce, *ApJ* **502**, 63 (1998).
22. A. R. Cooray, J. M. Quashnock, M. C. Miller, *ApJ* **511**, 562 (1999).
23. G. Golse, J.-P. Kneib, G. Soucail, *A&A* **387**, 788 (2002).
24. M. Sereno, *A&A* **393**, 757 (2002).
25. G. Soucail, J.-P. Kneib, G. Golse, *A&A* **417**, L33 (2004).
26. J. Gilmore, P. Natarajan, *MNRAS* **396**, 354 (2009).
27. T. Broadhurst, N. Benítez, D. Coe, et al, *ApJ* **621**, 53 (2005).
28. M. Limousin, *et al.*, *ApJ* **668**, 643 (2007).
29. H. Ebeling, *et al.*, *MNRAS* **281**, 799 (1996).
30. O. Czoske, *IAU Colloq. 195: Outskirts of Galaxy Clusters: Intense Life in the Suburbs*, A. Diaferio, ed. (2004), pp. 183–187.
31. P. Natarajan, J.-P. Kneib, *MNRAS* **287**, 833 (1997).
32. P. Natarajan, *et al.*, *ApJ* **693**, 970 (2009).
33. S. H. Suyu, *et al.*, *ArXiv e-prints 0910.2773* (2009).
34. E. Jullo, *et al.*, *New Journal of Physics* **9**, 447 (2007).
35. V. Springel, C. S. Frenk, S. D. M. White, *Nature* **440**, 1137 (2006).
36. P. Natarajan, G. De Lucia, V. Springel, *MNRAS* **376**, 180 (2007).

37. R. Kessler, *et al.*, *ApJS* **185**, 32 (2009).
38. E. Komatsu, *et al.*, *ApJS* **180**, 330 (2009).
39. P. Astier, *et al.*, *A&A* **447**, 31 (2006).
40. A. Kassiola, I. Kovner, *ApJ* **417**, 450 (1993).
41. S. M. Faber, R. E. Jackson, *ApJ* **204**, 668 (1976).
42. S. Wuyts, P. G. van Dokkum, D. D. Kelson, M. Franx, G. D. Illingworth, *ApJ* **605**, 677 (2004).
43. A. Fritz, B. L. Ziegler, R. G. Bower, I. Smail, R. L. Davies, *MNRAS* **358**, 233 (2005).
44. L. V. E. Koopmans, T. Treu, A. S. Bolton, S. Burles, L. A. Moustakas, *ApJ* **649**, 599 (2006).
45. M. S. Turner, M. White, *Phys. Rev. D* **56**, 4439 (1997).
46. T. Broadhurst, *et al.*, *ApJ* **619**, L143 (2005).
47. M. Oguri, M. Takada, K. Umetsu, T. Broadhurst, *ApJ* **632**, 841 (2005).